



Magmatic platinum nanoparticles in metasomatic silicate glasses and sulfides from Patagonian mantle xenoliths

José María González-Jiménez¹ · Josep Roqué-Rosell^{2,3} · Abigail Jiménez-Franco^{2,3,4} · Santiago Tassara⁵ · Fernando Nieto^{1,6} · Fernando Gervilla^{1,6} · Sandra Baurier^{2,3} · Joaquín A. Proenza^{2,3} · Edward Saunders⁷ · Artur P. Deditius⁸ · Manuel Schilling⁹ · Alexandre Corgne⁹

Received: 2 January 2019 / Accepted: 3 May 2019 / Published online: 13 May 2019
© Springer-Verlag GmbH Germany, part of Springer Nature 2019

Abstract

Platinum-rich nanonuggets (*s.l.*, nanoparticles) are commonly produced in experiments attempting to quantify the solubility or partitioning of noble metals in silicate and sulfide melts. However, it has been thought that these represent artifacts produced during quenching of the experimental runs. Here, we document nanoparticles (~20–80 nm) of Pt-rich alloys and arsenides dispersed in high-temperature metasomatic silicate glasses and in base-metal sulfides (BMS) entrained in them, found interstitially between minerals of mantle peridotite xenoliths from southern Patagonia. Pt-rich nanoparticles found in the interstitial silicate glasses are frequently attached to, or in the proximities of, oxides (ilmenite or Cr-spinel) suggesting a close link between the formation of the oxides and the Pt-rich nanoparticles. The interstitial glasses in the studied xenoliths correspond to quenched alkaline basaltic melts that infiltrated the subcontinental lithospheric mantle (SCLM) at > 1000 °C at an oxygen fugacity (fO_2) near the fayalite–magnetite–quartz (FMQ) buffer. Experimental works indicate that at these conditions the crystallization of oxides such as ilmenite or Cr-spinel may lower fO_2 to promote the precipitation of Pt-rich nanoparticles. The investigation of four Pt-rich nanoparticles hosted in two different pentlandite grains using a combination of focused ion beam and high-resolution transmission electron microscopy (FIB/HRTEM) show that these nanoparticles consists of polycrystalline aggregates < 10 nm that are randomly oriented relative to their sulfide host matrices. These observations suggest that these nanoparticles could be segregated either directly from the infiltrating alkaline basaltic melt prior to sulfur saturation in the silicate melt, or from droplets of immiscible sulfide melt once sulfur saturation was achieved. The formation of Pt-rich nanoparticles in high-temperature melts, either silicate or sulfide, provides new clues on the processes of fractionation, transport and concentration of Pt in the mantle.

Keywords Nanoparticles · Platinum · Silicate glass · Sulfides · Focused ion beam (FIB) · Mantle xenoliths

Introduction

Experimental studies predict that during crystal fractionation of magmatic melts Pt will be concentrated along with the immiscible sulfide melt following the separation of a sulfide melt from a silicate magma at ~1200 °C, owing its

extremely high sulfide/silicate partition coefficient (Mungall and Brenan 2014). However, once sulfide melts crystallize, Pt will not be incorporated in their low-temperature solid products, i.e., monosulfide solid solution (MSS) and intermediate solid solution (ISS) (Liu and Brenan 2015). Instead, Pt forms platinum-group minerals (PGM), often from the residual immiscible semimetal-rich (As, Sb, Te, and Bi) melt left behind after the crystallization of the MSS and ISS (Holwell and McDonald 2010; Holwell et al. 2015). This “canonical” model, which explains the Pt zonation observed in many crustal-hosted magmatic sulfide deposits conflicts with the fact that similar Pt concentrations are detected in MSS, pentlandite and chalcopyrite coexisting in composite aggregates found in many mantle rocks (e.g., Alard et al. 2011; Lugué and Reisberg 2016). According to

Communicated by Chris Ballhaus.

Electronic supplementary material The online version of this article (<https://doi.org/10.1007/s00410-019-1583-5>) contains supplementary material, which is available to authorized users.

✉ José María González-Jiménez
jmgonzj@ugr.es

Extended author information available on the last page of the article

Aulbach et al. (2016), this discrepancy has been interpreted to reflect: (1) the post-magmatic modification of the PGE signature of the BMS through interaction with small volume of oxidizing, volatile-rich melts, or (2) reaction of (sub)-micrometric Pt-rich minerals present in the mantle peridotite with percolating Ni ± Fe ± Cu sulfide melts (i.e., resulfidised platinum-group minerals).

An alternative explanation is that Pt could be present in melts as nanoparticles in melts before the formation of the solid BMS, possibly as native metal or in combination with other metals like Fe or semimetals such as S, As, Te, and Bi. This hypothesis was originally proposed in the 1980s by researchers working on magmatic PGE “Reef-style” deposits associated with the large layered intrusions of the Bushveld Complex in South Africa and the Great Dyke of Zimbabwe (Wilson and Tredoux 1990; Tredoux et al. 1995; Ballhaus and Sylvester 2000). Recent observations by Helmy et al. (2013) in experiments involving As-bearing sulfide melts seem to provide support to this hypothesis. Additional evidence supporting the pre-nucleation hypothesis comes from identification of Pt-rich nanoparticles in pentlandites from the Bushveld Complex (Wirth et al. 2013; Junge et al. 2015) and the mantle-hosted chromitite deposit of Caridad in the eastern Cuban ophiolites (González-Jiménez and Reich 2017; González-Jiménez et al. 2018) using a combination of focused ion beam and high-resolution transmission electron microscopy (FIB/HRTEM). Pt-rich nanoparticles reported by Wirth et al. (2013) and Junge et al. (2015) from the Bushveld Complex are heterogeneously distributed with no structural control from the host pentlandite, which has led these authors to interpret that Pt-rich nanoparticles were formed early in the high-temperature silicate melt, instead as a result of low-temperature exsolution of Pt from the BMS. In this model, the pre-existing Pt-rich nanoparticles would act as nuclei for the adhesion of sulfide liquid droplets once the melt reached sulfide saturation.

Similarly, in the mantle-hosted chromite deposit of Caridad in Cuba, nanospherical inclusions (<250 nm) of Ir–Pt nanoparticles were found with no orientation dispersed through the matrix of the (Ru-rich) pentlandite, suggesting that their formation preceded the segregation of sulfide droplets in the basaltic melt (González-Jiménez et al. 2018). The experimental results by Amossé et al. (1990) and Borisov and Palme (1995) suggested that the formation of Ir–Pt nanoparticles is expected in the silicate melt due to the strong tendency of these two metals to form nuggets in high-temperature silicate melts (~1500–1200 °C). In the case of Caridad, this siderophile behavior of Ir and Pt was strongly reinforced by local changes in fO_2 produced in response to chromite crystallization, which promoted the incompatibility of these two noble metals in the basaltic melt. Additional support for this interpretation comes from the experimental results of Finnigan et al. (2008) where Ir–Pt nanocrystals similar in size to those observed in

pentlandites from the Caridad chromite deposits (~700 nm in diameter) crystallised directly from basaltic melt at the P – T – fO_2 conditions relevant for the formation of chromite deposits in the upper mantle, i.e., 0.5 GPa, $T \approx 1300$ – 1400 °C and fO_2 at FMQ.

All the aforementioned experimental and empirical observations seem to confirm that Pt-rich nanoparticles may be stable in high-temperature silicate and sulfide melts. However, textural evidence decisively supporting that Pt-rich nanoparticles commonly exist in these melts is still equivocal. For example, Wainwright et al. (2016) have reported (sub)-micrometric ($\ll 1 \mu\text{m}$) Pt–Fe alloys in partly altered pyrrhotite–pentlandite mixtures from a peridotite xenolith from the Bultfontein kimberlite, South Africa. The inspection of thin foils containing these nanoparticles under the TEM indicates that Pt-rich nanoalloys show a preferential orientation with respect to their sulfide matrices. Similarly, one FIB thin-foil analysed by González-Jiménez et al. (2018) in the mantle-hosted chromitite of Caridad in eastern Cuba contains Ir–Pt nanoparticle-forming domains within (Ru-rich) pentlandite. These nanostructural observations contradict the pre-nucleation theory, supporting the conventional thought that low-temperature exsolution inducing formation of discrete (sub)-micrometric particles of Pt (and other PGEs) in magmatic pentlandite. Pt could be retained within the structure of MSS, but as the temperature dropped and the MSS re-equilibrated into pentlandite ± pyrrhotite, the Pt will no longer be accommodated and will form separate minerals (e.g., Makovicky et al. 1986; Fonseca et al. 2009).

A reliable approach to elucidate the possible formation of nanoparticles in natural high-temperature melts is to study samples that have experienced little or no subsolidus re-equilibrium. Mantle xenoliths rapidly transported to the surface by basaltic magmas during volcanic eruptions usually preserve intact magmatic features, including quenched silicate glasses and sulfides entrained in them. These represent unique windows into high-temperature magmatic processes operating in nature. Here, we report the occurrence of Pt-rich nanoparticles in the solid products resulting from the quick crystallization of immiscible sulfide melt droplets and their host silicate magma, corresponding to glassy veins preserved in a set of mantle xenoliths. These glassy veins represent former silicate melts that had infiltrated a volume of subcontinental lithospheric mantle (SCLM) in Patagonia, southern South America. We explore the factors potentially responsible for Pt-rich nanoparticle formation in these well-characterised samples, providing clues for refining previous knowledge on Pt partitioning in high-temperature melts.

Geological and petrological background of the samples

Geological setting

The samples analysed in this study include five peridotite xenoliths hosted by alkaline basalts from the eruptive centers known as Gobernador Gregores and Cerro Redondo, located in the southwestern part of the Deseado Massif, southern Patagonia (Santa Cruz Province, Argentina; Fig. 1). These volcanic centers are located in a back-arc position with respect to the current Andean volcanic chain. These two xenolith localities lie within the basaltic plateau known as Meseta Central, ~250 km east of the volcanic gap between the Southern Volcanic Zone (SVZ) and the Austral Volcanic Zone (AVZ). The absence of volcanic activity in this region is attributed to subduction of the Chile ridge related to the present-day triple junction between the Nazca, South American and Antarctic plates at 46.3°S (Forsythe et al. 1986). In the back-arc region in Argentina an extensive volcanic province of Middle–Late Jurassic is known as the Chon Aike Large Igneous Province (CA-LIP). This volcanism has been related with the thermal impact caused by the Karoo mantle plume that produced tholeiitic magmatism at ~188 Ma, the subsequent break-up of Gondwana (187–144 Ma) and a late calc-alkaline stage ~155 Ma produced during the east-facing subduction of the Pacific plate beneath the western margin of Gondwana (Féraud et al. 1999; Pankhurst et al. 2000; Riley et al. 2001). The formation of the Deseado Massif auriferous

province is genetically related with the late stage of the CA-LIP (Tassara et al. 2017 and references therein). More recent magmatism in the area include Miocene (~14–5 Ma) plateau basalts of tholeiitic to alkaline composition and Pliocene (~6–2 Ma) post-plateau alkaline, OIB-like basalts occurring in volcanic centers, which are related with perturbations induced by the subducting slab in the deep lithospheric or asthenosphere levels of the mantle wedge (Stern et al. 1990).

At the Gobernador Gregores locality (48°47'S, 68°56'W; Fig. 1) mantle xenoliths occur as ejection products entrained in basanite alkaline basalt constituting a N–S aligned diatrema cutting through the basaltic plateau. Cerro Redondo (49°7'S, 70°8'W; Fig. 1) is located approximately 60 km south of Gobernador Gregores also in the Santa Cruz province of Argentina, in the southwestern corner of the Deseado Massif (Fig. 1). Cerro Redondo has a dome form, with a semicircular base of ~800 m in diameter and a height of ~300 m above alluvial deposits of the Chico River. This structure has been interpreted as an ancient cinder cone, now almost completely eroded, located over a sill that corresponds to a sub-volcanic magma chamber (Schilling et al. 2005). The ultramafic xenoliths are unaltered and dispersed in the basalt.

Samples

The peridotite xenoliths from Gobernador Gregores and Cerro Redondo have sampled different volumes of a relatively depleted subcontinental lithospheric mantle (SCLM) as old as 2.0 Ga (Schilling et al. 2008, 2017; Tassara et al. 2018), which records a protracted history of partial melting and infiltration by metasomatic agents of carbonatitic-like affinity and nepheline-normative alkali basalts (Laurora et al. 2001; Gorrington and Kay 2000; Schilling et al. 2005; Tassara et al. 2017, 2018). The samples used here are lherzolites from the localities of Gobernador Gregores (samples GG-14 and GG-17) and Cerro Redondo (samples CR-01, CR-07, and CR-08) of the Cr-diopside suite that equilibrated in the spinel facies (up to 1.75 GPa, ~53 km depth). The petrology of these xenoliths was studied in detail by Gorrington and Kay (2000), Laurora et al. (2001), Schilling et al. (2005), Scamberulli et al. (2009) and Tassara et al. (2017, 2018). These peridotite xenoliths are relatively large (up to 30 cm in diameter) and exhibit microgranular (Gobernador Gregores) to protogranular, granular, and porphyroblastic microstructures (Cerro Redondo). Estimation of the temperature of equilibration obtained from mineral pairs using the approaches of Brey and Köhler (1990), Köhler and Brey (1990) and Taylor (1998) carried out by Tassara et al. (2018) on the suite of samples used in this study indicates temperatures between 782 and 1076 °C for peridotites from Gobernador Gregores and between 962 and 1150 °C for peridotites from Cerro Redondo.

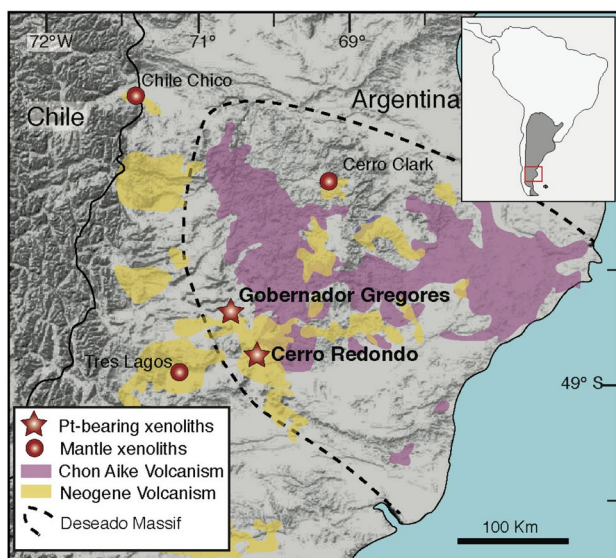


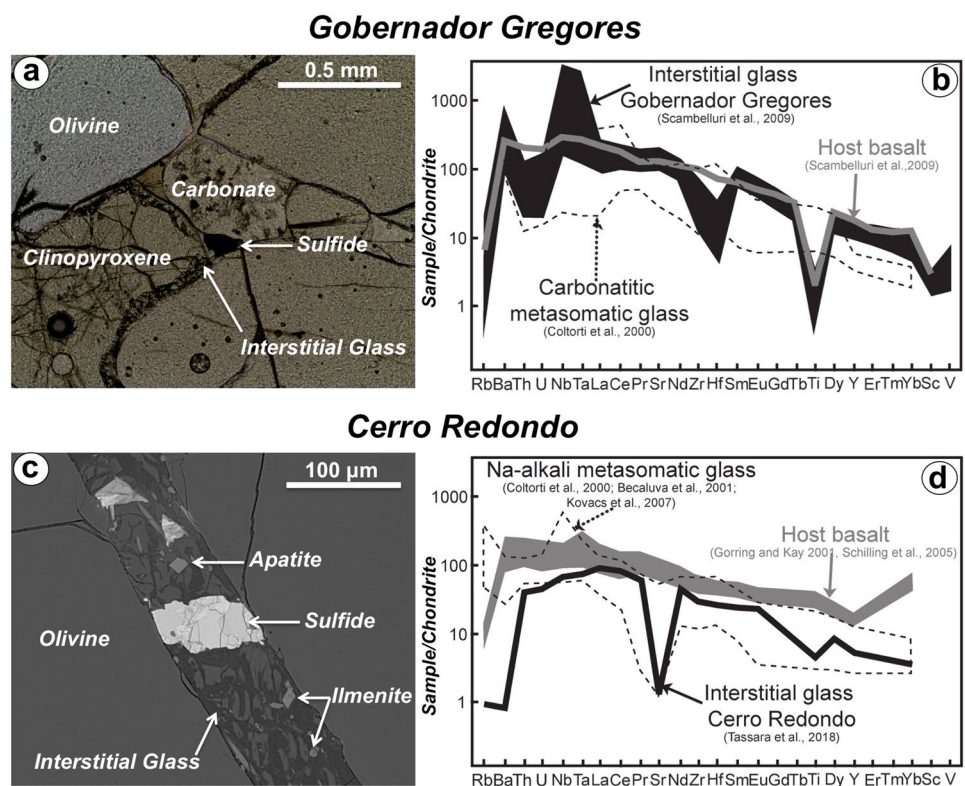
Fig. 1 Simplified geological map of southern Patagonia Argentina showing the two localities with xenoliths hosting Pt-rich nanonuggets (modified from Tassara et al. 2017). The dotted line marks the limits of the Deseado Massif auriferous province. Legend is inset in the map

The samples may contain accessory metasomatic minerals such as amphibole, phlogopite, carbonates, and apatite. The latter phases have been interpreted as evidence of metasomatism of the ancient Proterozoic SCLM by CO₂-rich (carbonatitic-like) melts evolving, after variable fluid-melt/rock ratio interaction, towards CO₂-rich and Na-bearing, Mg-rich (mafic) silicate melts and finally, volatile-rich alkali silicate melts (Laurora et al. 2001; Schilling et al. 2005; Scamberulli et al. 2009; Tassara et al. 2017, 2018). These metasomatised xenoliths are typically cross-cut by a suite of silicate glass veins that may form a discontinuous system of melt pockets surrounding amphibole and/or phlogopite (Gobernador Gregores) or interconnected network of veins cross-cutting the peridotite with sharp contact against the silicate matrix (Cerro Redondo). The geochemistry of major and trace elements and mineralogy of inclusions found in glasses in the studied peridotites from the Gobernador Gregores and the Cerro Redondo is distinctly different to the host basalt (Fig. 2), which is consistent with the fact that these glasses were never observed in connection with enclosing basalt. These glasses represent quenched melts that infiltrated the mantle just before xenolith exhumation during the extensive Neogene back-arc plateau magmatism at ~3.5 Ma ago (Tassara et al. 2018).

Laurora et al. (2001) and Scamberulli et al. 2009 analysed the composition of the carbonate-bearing glasses that occasionally surround amphibole and phlogopite in hydrous lherzolites from the Gobernador Gregores

(Fig. 2a, b) reporting that they have restricted ranges in SiO₂, respectively, corresponding to 50–53 wt% and about 55 wt%. The glass surrounding amphibole typically has higher Na₂O (8 wt%) contents than that surrounding phlogopite, which usually contains higher K₂O (5 wt%) and TiO₂ (3.5 wt%). LA-ICP-MS analysis carried out by Scamberulli et al. (2009) indicate that these glasses cross-cutting the hydrous peridotites of the Gobernador Gregores are characterised by marked positive Ba and Nb, Ta, and Sr spikes, coupled with negative Zr, Hf, and Ti anomaly. These signatures are similar to the amphiboles (Laurora et al. 2001), but are clearly distinct from those of the host basalt and commonly erupted alkaline lavas in Patagonia. The glassy veins at Cerro Redondo also exhibit a distribution of major, minor and trace elements very distinct from that of the host basalt. Tassara et al. (2018) have recently analysed these glasses showing that they have relatively high contents of SiO₂ (46.7–51.7 wt%), MgO (> 28 wt%) and Al₂O₃ (7.8–13.5 wt%) as well as primitive-normalised trace element pattern alike to Na-rich, silica undersaturated alkali melts (Fig. 2b, c). These glassy veins contain a mineral assemblage made up of a second generation of olivine coexisting with relicts of partly corroded pyroxenes associated with armalcolite, ilmenite, Na–K feldspar and apatite (Fig. 2b, c). These geochemical and mineralogical fingerprints have been related with the infiltration of highly alkaline melts, anomalously enriched in incompatible elements resulting from partial melting

Fig. 2 Representative textures, mineralogy, and composition of the interstitial glasses containing Pt-rich nanoparticles in the studied xenoliths. Trace element data for interstitial glass and host basalt of Gobernador Gregores are from Scamberulli et al. (2009) whereas those for interstitial glass of Cerro Redondo are from Tassara et al. (2018) and the host basalt from Goring and Kay (2000) and Schilling et al. (2005). Fields of glasses related to metasomatism by carbonatitic (Coltorti et al. 2000) and Na-alkali basaltic melts (Coltorti et al. 2000; Kovacs et al. 2008) reported from other mantle xenoliths are shown for comparison



of domains of the SCLM previously metasomatised by plume-related melts (Tassara et al. 2017).

Interestingly, in the two localities studied here the silicate glasses contain sulfide blebs ($\leq 150 \mu\text{m}$; Fig. 2) consisting of single grains or mixtures of monosulfide solid solution (MSS) \pm pentlandite $[(\text{Ni},\text{Fe})_9\text{S}_8] \pm$ millerite (NiS) \pm chalcopyrite (CuFeS_2). These are interpreted as droplets of Fe–Ni–Cu sulfide melt that were extracted from the surrounding peridotite during melt–rock reactions and later physically entrained by the infiltrating silicate melts now quenched as silicate glasses (Tassara et al. 2018).

Analytical procedures

Field emission scanning electron microscopy

All sulfide and platinum nanoparticles were imaged using two different instruments: a QUEMSCAN 650F Field Emission Gun Environmental Scanning Electron Microscope (FEG-ESEM) and Leo Gemini Field Emission Scanning Electron Microscope (FE-SEM) belonging to the *Centro de Instrumentación Científica* of the Universidad de Granada, Spain. These instruments are equipped with SE, BSE and EDS detectors. Accelerating voltage was 20 kV and beam current optimized for a sufficient number of counts for each EDS analysis. The EDS spectra representative of Pt-rich nanoparticles are provided in Appendix 1 in ESM.

Electron-microprobe analyses

The major and minor element composition of base-metal sulfides were acquired using a JEOL 8530F electron probe microanalyzer (EPMA) equipped with five tunable wavelength-dispersive spectrometers at the Centre of Microscopy, Characterization and Analysis (CMCA), University of Western Australia. Operating conditions were 40° take-off angle, an accelerating voltage of 20 kV, a beam current of 20 nA, with the beam fully focused. Elemental data were acquired during two analytical sessions. The following analysing crystals were used: LiF for Fe K α , Ru L α , Te L α , Cu K α , Ni K α , Co K α , Cr K α , Sn L α , Hg L α , Re L α , Os L α , Ir L α , Pt L α , PETJ for Rh L α , S K α , Ag L α , Pd L α , Ru L α , PETH for Mo L α , Pb M α , Sb L α , Bi M α , and TAP for Si K α , As L α , Se L α . The counting time was 20–30 s for all elements and Mean Atomic Number (MAN) background correction used for all elements (Donovan et al. 2016). The standards were Cr₂O₃ for Cr K α , galena for Pb M α , Bi₂Se₃ for Se L α , Ag for Ag L α , Cu metal for Cu K α , wollastonite for Si K α , Mo metal for Mo L α , Co metal for Co K α , Bi metal for Bi M α , Pt metal for Pt L α , elemental Sb for Sb L α , arsenopyrite (Asp200) for As L α , cassiterite for Sn L α , Au metal for Au L α , millerite for S K α , Ni K α , chalcopyrite for Fe K α , Ru metal for Ru L α , Rh metal for Rh L α , Pd metal for Pd

L α , Os metal for Os L α , Ir metal for Ir L α , Re metal for Re L α , and Synthetic HgTe (coloradoite) for Te L α , Hg L α . On peak interference corrections were applied as appropriate (Donovan et al. 1993). Unknown and standard intensities were corrected for deadtime. For both sessions, a quantitative blank correction was utilised. The Phi-Rho-Z algorithm utilised was Armstrong/Love Scott (Armstrong 1988). Data are provided in Appendix 2 in ESM.

Laser ablation-inductively coupled-mass spectrometry

Selected individual base-metal sulfides $> 50 \mu\text{m}$ in diameter were analysed for precious metals (Os, Ir, Ru, Rh, Pt, Pd, and Au). The analyses were carried out by LA–ICP–MS at the Geochemical Analysis Unit (GAU) at CCFS/GEMOC, Macquarie University, Sydney. Helium was used as the carrier gas, which was blended with Ar prior to introduction into the plasma. The laser ablation system was operated at 5 Hz with an average beam energy of 6.9 mJ per pulse. Sulphur, determined by EMP, was used as an internal standard for quantifying the trace element abundances. The isotopes monitored during LA–ICP–MS analysis were: ²⁹Si, ³¹P, ³⁴S, ⁴⁷Ti, ⁵⁵Mn, ⁵⁷Fe, ⁵⁹Co, ⁶⁰Ni, ⁶²Ni, ⁶³Cu, ⁶⁵Cu, ⁶⁶Zn, ⁷⁵As, ⁷⁸Se, ⁸²Se, ⁹³Nb, ⁹⁹Ru, ¹⁰¹Ru, ¹⁰³Rh, ¹⁰⁵Pd, ¹⁰⁷Ag, ¹¹¹Cd, ¹¹²Cd, ¹¹⁵In, ¹²¹Sb, ¹²⁵Te, ¹⁷²Yb, ¹⁸²W, ¹⁸⁵Re, ¹⁸⁹Os, ¹⁹³Ir, ¹⁹⁵Pt, ¹⁹⁷Au, ²⁰⁸Pb, ²⁰⁹Bi. For every run of approximately 10 sulfide grains, we analysed 3 standards (NIST610, PGE-A and IMER-2) each of which are analysed twice at the start of the run, and again twice at the end of the run. We also analysed the BCR-2 glass as an unknown. We used the NIST610 as a calibration standard to check the BCR-2 data; this lets us look at a broad range of atomic masses to ensure the instrument calibration was appropriate. However, the matrix of this standard is not well matched to a sulfide grain. We then use PGE-A (a quenched NiS doped with selected chalcophile and siderophile; Alard et al. 2000, 2002; Saunders et al. 2016) as an internal standard, and check the calibration against IMER-2, this gives us more confidence in the chalcophile/siderophile element calibrations (because the matrix of these two standards is far closer to that of a sulfide than the NIST glass). Additionally, we crosschecked PGE-A as an unknown using IMER-2 as a calibration standard. After all this, the analyses of the “unknown” sulfide grains were calibrated using PGE-A (except for Sb, which is calibrated using the IMER-2 data). No correlation between Cu and Rh, Cu and Pd or Ni and Ru was indicating no production of Cu⁶³Ar⁴⁰ (= Rh¹⁰³); Cu⁶⁵Ar⁴⁰ (= Pd¹⁰⁵) nor Ni⁶¹Ar⁴⁰ (= Ru¹⁰¹). Therefore, we made no corrections for isobaric these potential overlaps. Detection limits for LA–ICP–MS analyses are calculated as average background concentrations. The results, including limit of detection for each element and standard deviations are listed in Appendix 3 in ESM.

Thin-foil preparation, extraction, and observation by focused ion beam and high-resolution transmission electron microscopy

Electro-transparent thin-foil samples were prepared and extracted from selected base-metal sulfides where Pt-rich nanoparticles were previously identified using FE-SEM using a Focus Ion Beam Scanning Electron Microscope (FIB-SEM) Zeiss® Neon40 at the Research Centre in Multiscale Science and Engineering of the UPC (Polytechnical University of Catalonia) in Spain. First, the region of interest containing particles was coated with a silicon protective layer and subsequently the sample was milled by means of Ga ion bombardment until a $10 \times 15 \mu\text{m}$ thin-foil was dug in the base-metal sulfide. The thin-foil samples were extracted, welded to a Cu TEM grid and thinned down to an electron transparent thickness (down to $\sim 80 \text{ nm}$).

Subsequently the thin-foil samples were first analysed using a 200 kV TEM JEOL JEM 2100 LaB6 (JEOL Ltd., Tokyo) to perform EDS microanalysis and elemental mappings. The X-ray maps and spectra were recorded using an X-ray microanalysis INCA ultrathin window Si(Li) detector by Oxford Instruments. These thin-foil samples (sample GG-14) were further analysed using FEI Titan G2 transmission electron microscope (TEM) equipped with Field Emission cannon XFEG, with spherical correction for the objective lens and working at 300 kV belonging to the Centro de Instrumentación Científica de la Universidad de Granada, Spain. The microscope was equipped with four energy-dispersive analysis of X-rays (EDX) detectors (FEI microanalysis Super X) and high angle-annular dark field detector (HAADF). High-magnification electron microscopy images (HMEM) and High-Resolution Transmission Electron Images (HRTEM) were acquired using Gatan CCD Camera. The EDX allowed to perform elemental maps and microanalysis from areas and points of interest, the HAADF allowed to obtain Z high-contrast images, the HMEM allowed the texture characterization of the grain of study and HRTEM the ordering of the aggregates. The obtained images were subsequently processed with Digital Micrograph® Version 1.71.38 and maps with INCA® Microanalysis Suite version 4.09 software package.

Results

Pt-rich nanoparticles in silicate glasses and in entrained sulfides

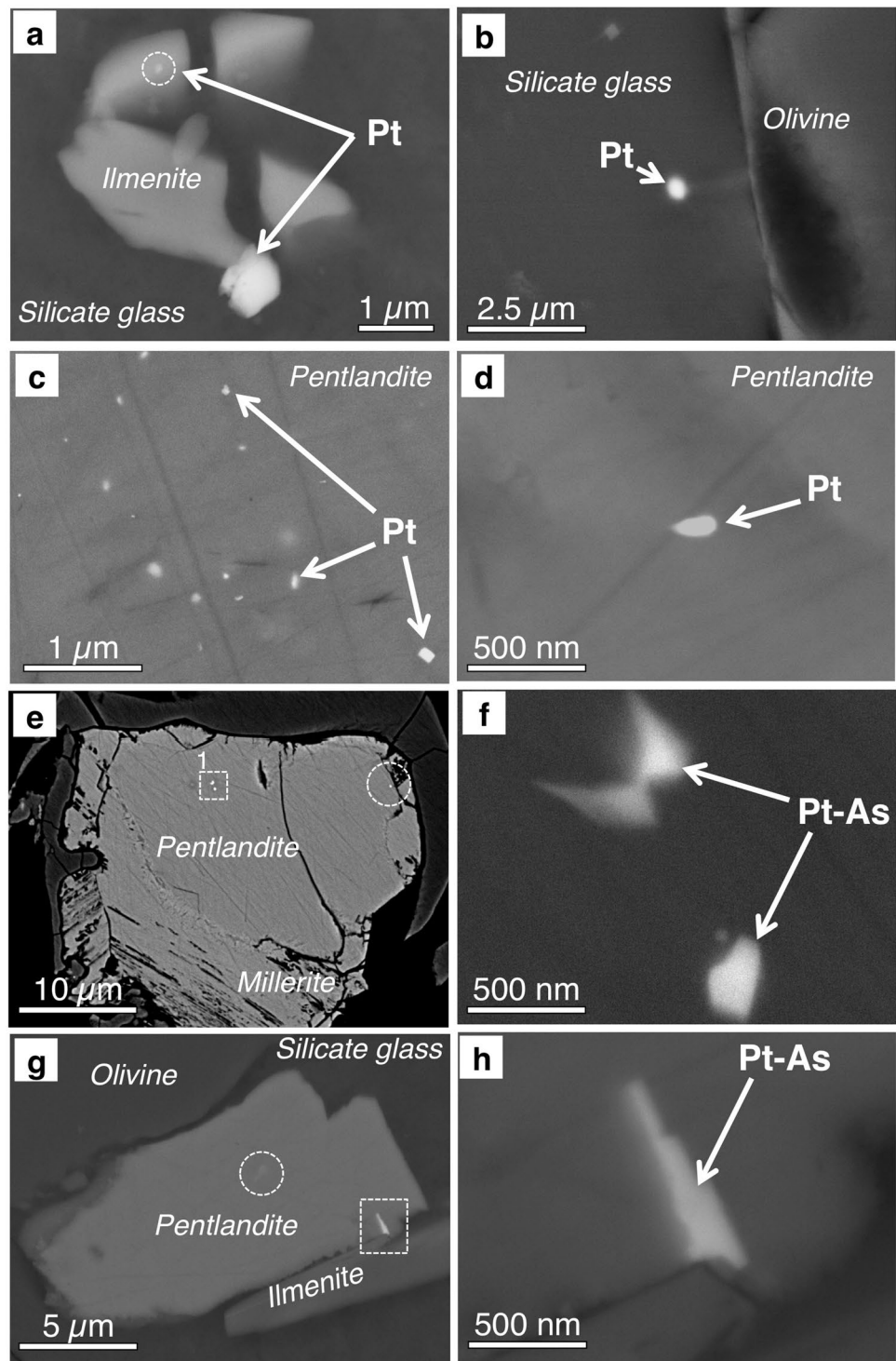
Several Pt-rich submicrometric ($< 1 \mu\text{m}$) particles were found in the glass matrix or in BMS entrained in the interstitial silicate glass from the Gobernador Gregores and the Cerro Redondo mantle xenoliths (Fig. 3a–h). Their

EDS spectra obtained using FESEM and filtered for host matrix composition indicate that these are almost pure Pt, Pt–Fe–Cu and Pt–As (Appendix 1 in ESM), although many of them were too small for reliable quantitative analyses. The arsenic-free, Pt-rich nanoparticles are embedded in the interstitial glass or hosted in BMS entrained in such interstitial glass (Fig. 3a–d; Appendix 1 in ESM). When occurring in the interstitial glass the latter Pt-rich nanoparticles may be found as single isolated crystals or attached to larger ilmenite grains (Fig. 3a; Appendix 1 in ESM). These latter nanoparticles exhibit the characteristic feature of well-developed polygonal faces towards the contact with the silicate glass (Fig. 3a; Appendix 1 in ESM). Arsenic-free, Pt-rich nanoparticles hosted in the BMS also tend to display well-developed morphologies. In contrast, the Pt–As nanoparticles were found exclusively associated with BMS. These latter nanoparticles exhibit both irregular and well-developed outlines (Fig. 3e–h; Appendix 1 in ESM).

The distribution of BMS carrying nanoparticles in the interstitial glass of peridotite xenoliths from Gobernador Gregores and Cerro Redondo is quite heterogeneous within a single sample. Thus, few grains containing these Pt-rich nanoparticles may coexist with other BMS lacking of these nanoparticles visible under the FESEM. Electron microprobe analysis of the BMS containing Pt-rich nanoparticles does not reveal significant differences in terms of major elements (Ni, Fe, Cu, S). These nanoparticles can be found in MSS, pentlandite or millerite found either as single grains or forming composite aggregates among them or with chalcopyrite (Appendix 2 in ESM). Pt-rich nanoparticles are preferentially concentrated in Ni–Fe sulfides and were not observed to be included in the Cu-rich sulfide chalcopyrite.

The LAM–ICPMS analysis of > 10 selected sulfide grains ($\geq 50 \mu\text{m}$ in diameter) hosting Pt-rich nanoparticles reveal that these types of sulfides show larger variations of the PGEs (Os: 2.43–32.6 ppm; Ir: 2.28–24.91 ppm; Ru: 5.83–58.92 ppm; Rh: 0.99–19.45 ppm; Pt: 0.11–0.5 ppm; Pd: 9.28–135.66 ppm) than those BMS free of Pt-rich nanoparticles (Os: 6.68–10.65 ppm; Ir: 6.57–10.39 ppm; Ru: 7.66–13.23 ppm; Rh: 2.47–4.98 ppm; Pt: 12.76–19.52 ppm; Pd: 12.22–22.88 ppm). These values produce similar flat or gently positive PGE-chondrite normalised patterns, although BMS carrying Pt-rich nanoparticles are characterised by a pronounced negative Pt anomaly (Fig. 4; Appendix 3 in ESM). In addition, careful examination of the time-resolved spectra signals collected during LA–ICP–MS analysis of the sulfides revealed the presence of abundant Pt and Cu spikes; this observation is consistent with BSE images and EDS spectra obtained using FESEM suggesting that Pt-rich nanoparticles are embedded within the sulfide matrix (Fig. 5).

Fig. 3 Back-scattered electron images of Pt-rich nanoparticles from distinct microstructural positions in the studied Patagonian mantle xenoliths. **a** and **b** Pt⁰ nanoparticles in the interstitial silicate glass from Cerro Redondo. **c** and **d** Pt-(Fe-Cu) nanoalloys in pentlandite hosted in interstitial silicate glass of Gobernador Gregores. **e-h** Pt-As nanoparticles in pentlandite from Cerro Redondo



Characterization of the Pt-rich nanoparticles in sulfides using FIB/TEM

Selected grains of MSS, pentlandite and millerite from Gobernador Gregores and Cerro Redondo xenolith hosting Pt-rich nanoparticles visible under the FESEM were sectioned with focused ion beam (FIB) technique to obtain ~70 nm

thin foil samples to be examined by TEM and HRTEM. Two of these thin-foils performed on two different pentlandite grains successfully intersected Pt-rich nanoparticles (Figs. 6, 7, 8, 9, 10).

One FIB thin-foil cut through a large grain of pentlandite hosted in the interstitial glass from a Gobernador Gregores xenolith (sample GG-14) intersected three

Fig. 4 CI chondrite-normalised platinum-group element patterns of the mixtures of MSS \pm pentlandite \pm millerite \pm chalcopyrite from the studied Patagonian mantle xenoliths and selected samples worldwide. Note that the plots include BMS with “visible” or “suspected” Pt-rich nanonuggets (by spikes in LA-ICP-MS time-resolved spectra) and neighbouring BMS lacking of them. Data for Montferrier xenolith are from Alard et al. (2011) and for Spitsbergen from Saunders et al. (2015)

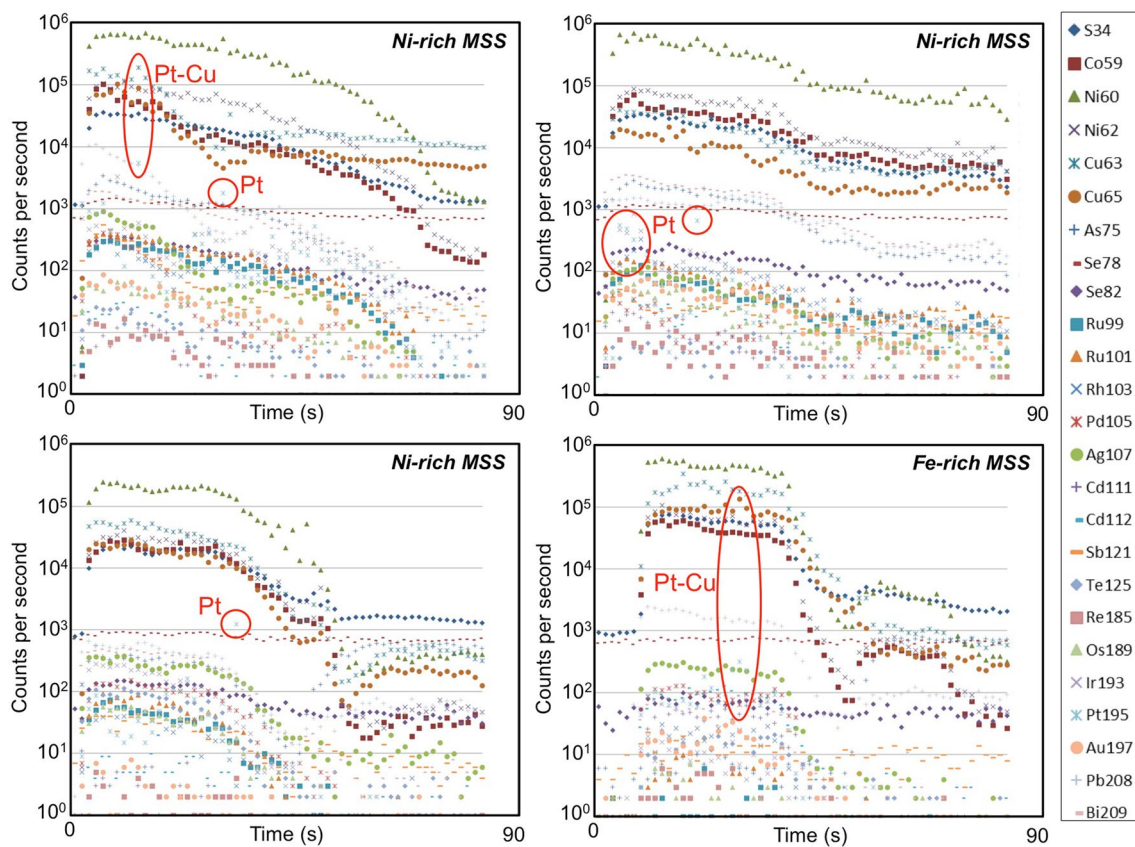
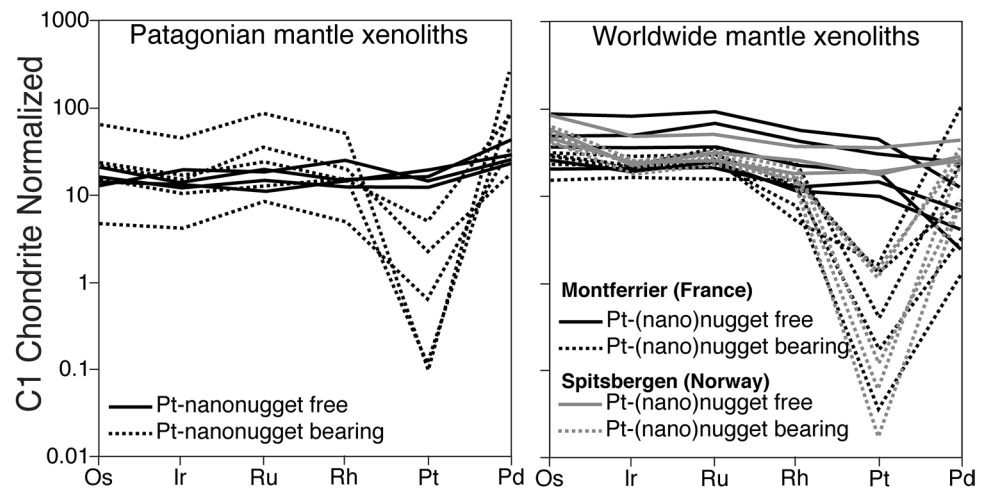


Fig. 5 Representative time-resolved LA-ICP-MS spectra collected during noble metal analysis of base-metal sulfides. The transient spectrum of ^{195}Pt spikes is interpreted as Pt-bearing inclusions

nanoparticles (Fig. 6): one that was observed from the surface cross section (the particle enclosed in the dotted rectangle A shown in Fig. 6), and two more deeply buried inside the pentlandite (particles enclosed in the rectangles B and C in Fig. 6). The high-magnification images (HMTEM) obtained from the three particles revealed that they range in size from ~ 20 to 80 nm across (Fig. 7a–c).

Energy-dispersive single-spot analyses and EDS elemental mapping obtained for each one of these three particles revealed that these particles contains varying proportions of Pt, Cu and Fe (Fig. 7a–c), although there is a lack of relative decrease of Pt, Cu, Fe, and Ni concentration in these nanoparticles towards the matrix consisting of Fe, Ni, and S. The obtained HRTEM images of

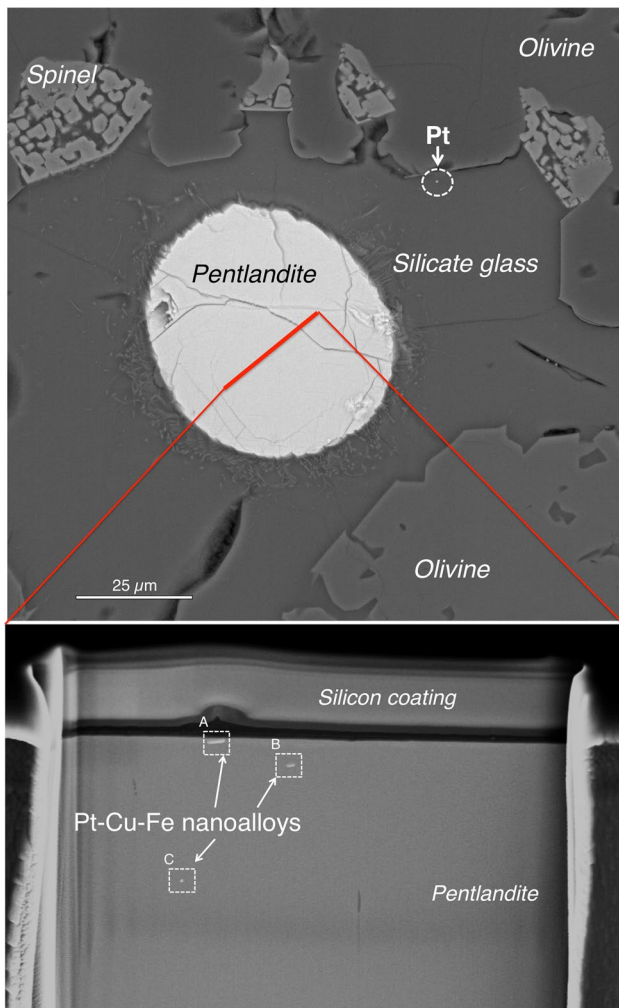


Fig. 6 Back-scattered images of thin-foil sampled from a pentlandite grain included within interstitial silicate glass from a Gobernador Gregores xenolith. The three nanoparticles of Pt–Fe–Cu intersected during sample preparation are enclosed in the rectangles and named as shown in Figs. 7 and 8

the two elongated particles (particles A and B in Figs. 7 and 8) indicate that they do consist of an aggregation of smaller crystalline domains. The corresponding selected area electron diffraction (SAED) patterns allow us to identify these crystalline domains as tulameenite (Pt_2CuFe) and hongshiite (PtCu) being randomly orientated within a pentlandite single crystal (Fig. 8a–b; Table 1). In addition, the FFT patterns obtained from a third nanoparticle (particle C in Figs. 6, 7 and 8) also allowed identification of pentlandite with the corresponding d-spacing (311) and (331) and two additional spacings at 4.48 Å and 9.2 Å (Fig. 8c). The value 4.48 Å is close to the d-spacing values reported for hongshiite by Ding (1980) and Kwitko et al. (2002), whereas the spacing 9.2 Å is thought to correspond to Moiré fringes resulting from the interference of pentlandite (311) and 4.48 Å d-spacing. Despite lacking

single crystal information from hongshiite (Kwitko et al. 2002), the presence of Moiré fringes confirms the well-crystallised nature of the Pt–Cu nanoparticle.

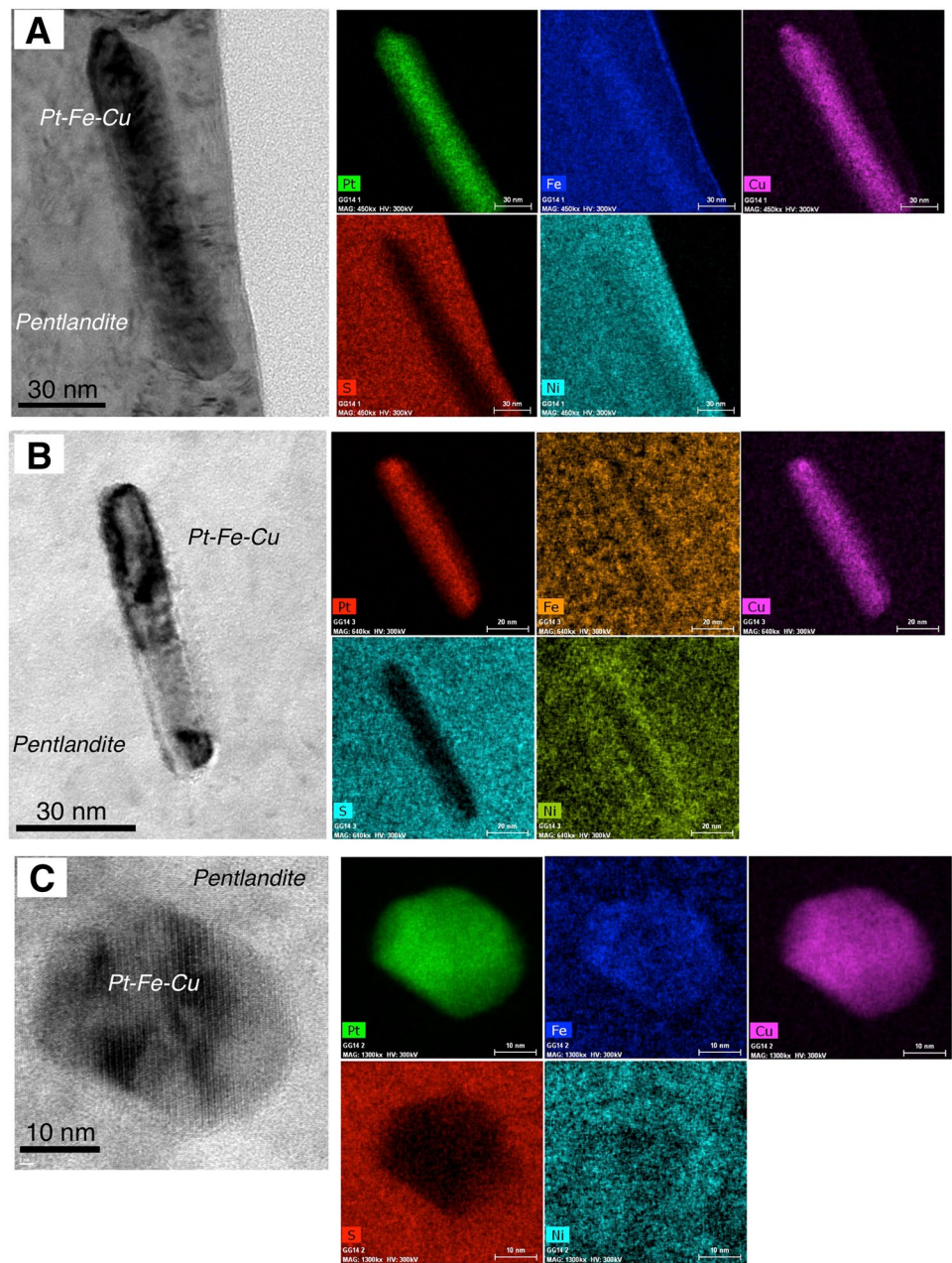
The second thin foil that successfully intersected two Pt-rich nanoparticles was obtained from a pentlandite grain hosted in a glassy vein from a Cerro Redondo xenolith (sample CR-07; Fig. 9). The smaller particle (namely A in Fig. 9) with a lower absorption contrast in HRTEM images is fully embedded deep in the sulfide matrix. The chemical microanalysis proved to be difficult but Pt was identified on this particle. The larger Pt-rich particle (namely B in Fig. 9) is ~ 60 nm long, subhedral and crystalline displaying a 2.374 Å d-spacing coincident with the (111) metallic Pt (Fig. 10; Table 2). Where the nanoparticle is embedded within the pentlandite matrix (identified by the 2.895 Å and 3.564 Å d-spacing corresponding to pentlandite (222) and (220), respectively) shows 4.78 Å and 6.34 Å Moiré fringes. No gradational change in the contents of Pt, Fe, and Ni is noted relative to the crystalline pentlandite host (Fig. 10), whereas significant misorientation [$\text{Pt (111)} \Delta \text{Pn (220)} = 14.62^\circ$] is observed between the lattices corresponding to the metallic Pt nanoparticle and the pentlandite host (both isometric with space group F m3m) (Table 2).

Discussion

The roles of oxides for the crystallization of Pt-rich nanoparticles

Experimental studies have reported the formation Pt and Pt–Fe nanoparticles at > 1000 °C from Fe-bearing/free and S-free/undersaturated basaltic melts buffered with $f\text{O}_2$ near the fayalite–magnetite–quartz (FMQ) buffer (Borisov and Palme 1997; Ertel et al. 2006; Médar et al. 2015; Anenburg and Mavrogenes 2016). At the relatively high $f\text{O}_2$ values of the FMQ buffer, the solubility of Pt in basaltic melts lacking S or undersaturated respect S is relatively insensitive to the composition of the basaltic melt but is quite sensitive to variations in $f\text{O}_2$. At these given conditions, the solubility of Pt in most terrestrial basaltic melts is controlled by the Pt^{2+} oxide species instead of metal–sulfide (Bennet et al. 2014; Médar et al. 2015). Therefore, any local decrease in $f\text{O}_2$ of the melt may enhance reduction of the platinum dissolved as Pt^{2+} to Pt^0 thus promoting its saturation in the form of Pt-rich alloy nanoparticles (Borisov and Palme 2000; Amossé et al. 2000; Ballhaus et al. 2006; Médar et al. 2015). The results of experimental (Ballhaus et al. 2006; Finnigan et al. 2008; Anenburg and Mavrogenes 2016) and empirical works (Roeder and Jamieson 1992; Kamenetsky et al. 2015; Arguin et al. 2016) indicate that this siderophile behavior is strongly reinforced when oxides crystallize from the silicate melts, as

Fig. 7 EDS maps obtained using HRTEM of the three Pt–Fe–Cu nanoparticles included in pentlandite shown in Figs. 6 and 8. Each nanoparticle is named A, B and C as in Figs. 6 and 8



these should lower the fO_2 down enough to affect the stability of Pt in the silicate melts.

Scamberulli et al. (2009) reported that interstitial vein glasses in the hydrous xenoliths of Gobernador Gregores were produced by the reaction of an infiltrating alkali melt with the local mineral assemblage (mainly amphibole) of a relatively more oxidized peridotite in a range of ΔFMQ between -0.35 and 0.05 at temperatures ranging from 1064 to 998 °C and at 1.6 GPa. Recently, Tassara et al. (2017) suggested that the infiltrating alkali melt, now quenched as interstitial glass in a Cerro Redondo mantle xenolith, was slightly more reduced than the FMQ ($\Delta FMQ \approx -2.35$ at temperatures ranging from 1150 to 1200 °C and at 1.3 GPa)

and the primary silicates infiltrating the host peridotite ($\Delta FMQ \approx 0.12$ to 1.06). These estimates reflect the infiltration of an alkali melt buffered with fO_2 close or approaching to the values of the FMQ buffer. According to the experiments cited above this is a favorable scenario for the precipitation of Pt-rich nanoalloys. In a melt with Pt preferentially dissolved an oxide species, the local perturbations in fO_2 necessary for the precipitation of Pt as nanoparticles could be achieved at the melt–solid interfaces between silicates (e.g., secondary pyroxene or olivine) and Fe–Ti–Cr-oxides (ilmenite and Cr-spinel) (re)-crystallizing in the melt or at the melt-wall rock during infiltration of the alkali melt. This may explain why many of the Pt-rich alloy nanoparticles

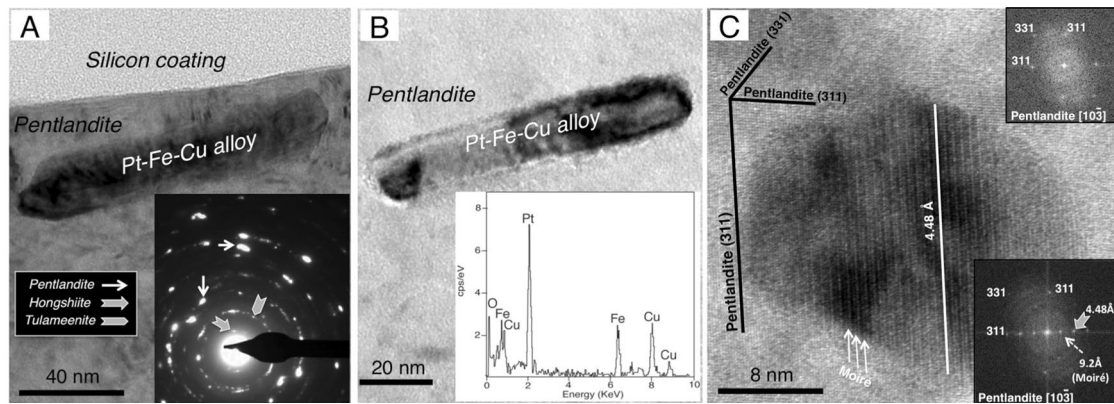


Fig. 8 HRTEM images of nano-sized particles of Pt–Fe–Cu alloys in pentlandite shown in Figs. 6 and 7. Insets include: **a** Selected area diffraction pattern of the nanoparticles and host pentlandite for the nanoparticle A, **b** EDX spectra of the Pt–Fe–Cu alloys for the nanoparticle B, and **c** Fast Fourier Transform (FFT) of high-resolution image showing main diffraction maxima and Miller indices for the nanoparticle C

detected in our samples are located along the contacts between the interstitial silicate glass and primary silicates of the peridotite close to Cr-spinel (Figs. 3b and 8) or directly included or attached to ilmenite (Fig. 3a; Appendix 1 in ESM). In addition, the presence of Pt and Fe coupled in the nanoparticles suggests that the latter acted as an additional redox partner aiding the redox reaction that promoted the precipitation of Pt from the silicate melt. Although the results of many experiments predicted that Pt-rich nanoparticles could in practice form through oversaturation along with any other transition element (e.g., Cu; Médar et al. 2015) or PGE (e.g., Ir; Borisov and Palme 1997), the presence of iron in our nanoparticles seems to confirm previous experimental works indicating that a selective complexing of Pt with Fe might be a key step for the formation of Pt-rich nanoparticles in basaltic melts (e.g., Cottrell and Walker 2006).

The observation that Pt-rich nanoalloys associated with oxides in the samples studied here exhibit well-developed polygonal faces towards the contact with the silicate glass (Fig. 3a; Appendix 1 in ESM) also indicates that these nanoparticles achieved equilibrium with the ambient silicate melt while infiltrating the wall-rock peridotite in the upper mantle. The fact that some of these Pt-rich nanoparticles are included in ilmenite grains (Fig. 3a; Appendix 1 in ESM) suggests their formation prior or contemporaneously to the oxide formation. Further, the presence of other nanoparticles along the boundaries of larger ilmenite microphenocrysts embedded in the interstitial glass (Fig. 3a; Appendix 1 in ESM) could represent the first stage of the Pt-rich nanoparticle entrapment mechanism. Interestingly, the Pt-rich alloy nanoparticles shown on Fig. 3a exhibit morphologies and nanostructural relationships with the oxide similar to those observed for Pt-rich nanoparticles that have crystallised from synthetic alkaline basaltic melt in slow-cooling experiments (see Fig. 5e in Anenburg and Mavrogenes 2016), thus

providing a natural example for the mechanism of precipitation of Pt nanoparticles particles at the oxide–melt interface. Additionally, these observations confirm that Pt-rich nanoparticles within the interstitial silicate glass of the studied Patagonian mantle xenolith crystallised freely in the silicate melt and therefore they were not produced as a result of quenching of the hosting glass. Interestingly, Barnes et al. (2016) have reported micron-sized Pt-rich alloys and arsenides precipitated directly from the basaltic melt that originated Pt-rich pyroxenites from the Monts de Cristal Layered Complex in Gabon. In our case, after their formation, the chance of preservation of the Pt-rich nanoparticle would increase if they became isolated in, or attached to, larger oxide minerals that would protect them from the ongoing reactions with non-equilibrium surrounding silicate melt. The preservation of the nanoparticles found isolated within the interstitial glass could also reflect the very low equilibrium solubility of Pt in the alkali melt. In this scenario, detachment of a Pt atom from the metallic nanoparticle and/or diffusion into the silicate melt is hampered, as only a very small number of atoms is dissolved and may diffuse at any given time (Médar et al. 2015). The lower equilibrium concentration favors the preservation of the nanoparticles, as observed in many experimental studies (e.g., Ertel et al. 2008).

Stability of Pt-rich nanoalloys at sulfide saturation

The droplet-like morphology of BMS found in the interstitial silicate glass of the studied xenoliths (Fig. 6) indicates that they correspond to quenched droplets of immiscible sulfide melt that remained entrained in the infiltrating silica undersaturated, Na-rich alkaline melts just before the eruption of the xenolith. These droplets could be either be segregated to the infiltrating alkaline magma because

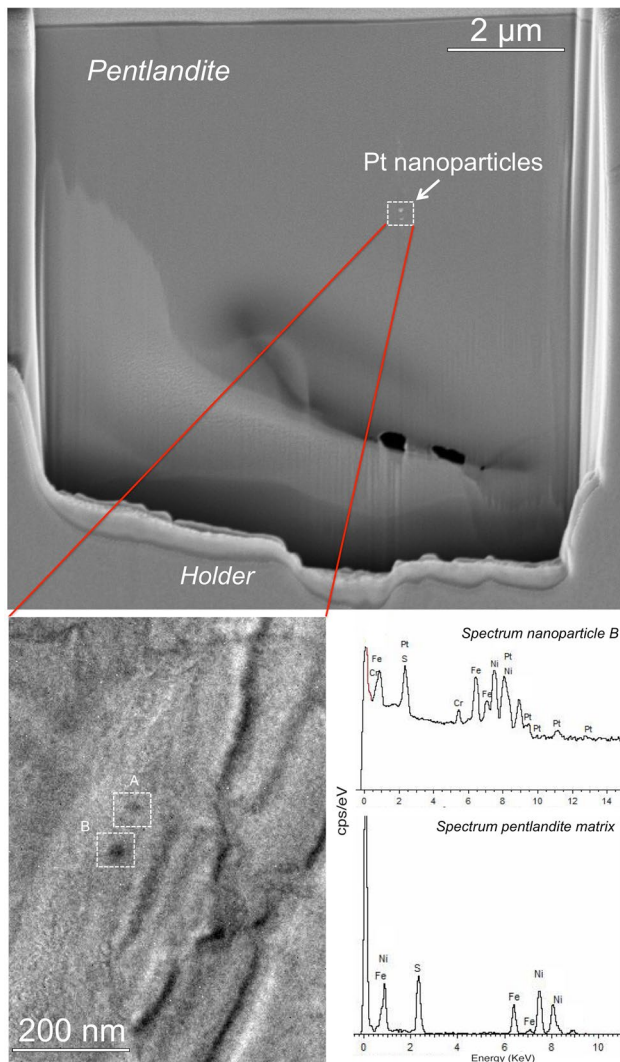


Fig. 9 Back-scattered images of thin-foil sampled from a pentlandite grain included within interstitial silicate glass from a Cerro Redondo xenolith. The two nanoparticles of Pt–Fe–Cu intersected during sample preparation are enclosed in the rectangles named as A and B

of melt–rock reactions elsewhere in the upper mantle, or alternatively be exsolved upon degassing and quenched due to rapid undercooling of the ascending xenolith. These two processes may reflect the local changes in fO_2 and fS_2 that may have also shifted the balance between the stability of the more-soluble sulfate towards less-soluble sulfide allowing the segregation of small droplets of immiscible sulfide melt in different mantle conduits. Small droplets of immiscible sulfide melts enriched in Ni, Cu, Fe and PGEs were segregated at high temperature (> 1000 °C) from the infiltrating alkali silicate melt now quenched as interstitial glass. This is also consistent with their relatively high PGE contents detected in single-spot analyses obtained using EPMA and LA–ICP–MS of some of the BMS (Fig. 4; Appendices 2 and 3 in ESM). These BMS occurring in the glass exhibit

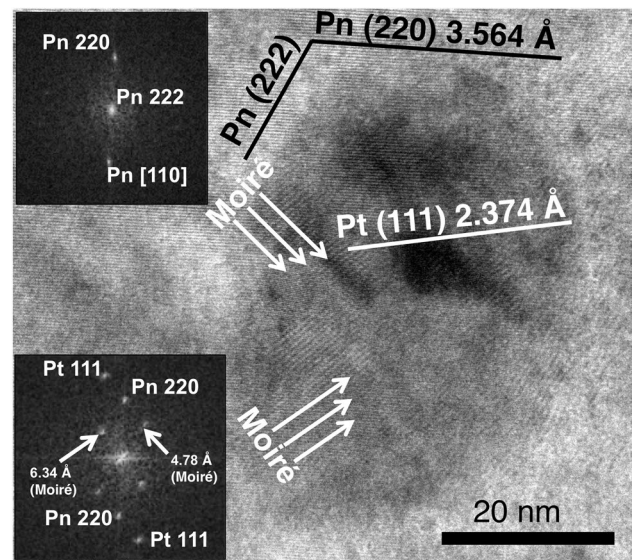


Fig. 10 HRTEM image of the nanoparticle of native platinum (nanoparticle B shown in Fig. 9) hosted in pentlandite from a Cerro Redondo xenolith. Insets include: Fast Fourier Transform (FFT) of high-resolution image showing main diffraction maxima and Miller indices for the nanoparticle obtained by HRTEM of the nanoparticle

distinctively near flat CI-chondrite PGE normalised patterns (Fig. 4), which is a typical signature of mantle BMS derived from the direct crystallization of Ni–Fe–Cu sulfide melts originated by unmixing from mafic melts (Wang et al. 2009; Lorand et al. 2010, 2013; González-Jiménez et al. 2014). Upon cooling (~ 1000 °C) the sulfide liquid first crystallised as MSS, and once temperature cooled down to $T < 600$ °C it re-equilibrated into lower-temperature sulfide assemblages consisting of MSS \pm pentlandite \pm millerite \pm chalcocopyrite (Craig and Kullerud 1969; Fleet and Pan 1994; Ballhaus et al. 2001). Alternatively, if MSS and the coexisting sulphide liquid enriched in Cu and Ni were not separated, they could react forming a high-temperature form of pentlandite via a peritectic reaction (Mansur et al. 2019). The results of several experimental studies (Sugaki and Kitakaze 1998; Waldner and Pelton 2004; Kosyakov and Sinyakova 2012; Kitakaze et al. 2016) indicate that high-temperature form of pentlandite can be produced as a result of the peritectic reaction between *mss* and Ni-rich liquid in the Ni–Fe–S system at ~ 870 °C, and it keeps growing from the sulfide liquid below the peritectic temperature down to 739 °C, becoming re-equilibrated at temperatures below 650 °C into the low-form of pentlandite. Moreover, metal–sulfide equilibrium in the Ni–Fe–S system (Wood 1987) indicates that the high-temperature polymorph of millerite α -NiS is stable at temperatures between 1000 and 1200 °C and a low sulfur fugacity ($\log fS_2$ from -0.5 to 1) relevant for the formation of Na–alkali metasomatic glass. The early crystallization of this α -NiS directly from melts can also explain the presence

Table 1 Indexed SAED pattern obtained from Pt–Fe–Cu nanoparticles shown in Fig. 8a

d-spacing (Å)	Pentlandite d-spacing (Å)	(<i>h k l</i>)	Tulameenite d-spacing (Å)	(<i>h k l</i>)	Hongshiite d-spacing (Å)	(<i>h k l</i>)
5.95	(0.06)	–	–	–	6.06	n/a
3.58	(0)	–	–	–	–	–
3.02	(0.05)	3.55	220	–	–	–
2.81	(0.12)	–	–	2.75	100	–
2.15	(0.03)	–	–	2.18	101	2.19
2.05	(0)	2.05	422	–	–	–
1.95	(0.04)	1.93	511	–	–	–
1.87	(0.02)	–	–	–	1.88	404
1.73	(0.02)	1.77	440	–	–	–
1.52	(0)	1.53	533	–	–	–
1.49	(0.02)	1.45	444	–	–	–
1.31	(0)	1.31	553	–	–	–
1.26	(0.04)	–	–	1.28	201	–
1.12	(0.02)	1.16	555	–	–	–

of millerite crystals associated or not with other BMS in the interstitial silicate glass as observed in our xenoliths.

The fact that BMS lacking “visible” Pt-rich nanoparticles exhibits flat PGE-chondrite normalised patterns (Fig. 4a) suggests that some droplets of immiscible sulfide melt segregated at this stage collected all PGE almost equally, in agreement with their similar extremely high sulfide/silicate partition coefficient (Li et al. 1996; Mungall and Brenan 2014; Liu and Brenan 2015). It contrasts with the observation that neighboring BMS hosting Pt-rich alloy nanoparticles also displaying nearly flat PGE–chondrite-normalised patterns exhibit a characteristic negative Pt anomaly (Fig. 4a). Interestingly, mixtures of pentlandite ± MSS (± Cu sulfides) having PGE-chondrite patterns exhibiting a flat slope with or without Pt anomaly have already been described in many other mantle xenoliths (e.g., Alard et al. 2011; Saunders et al. 2015). The negative Pt anomalies in these sulfides were interpreted to be a volume-sampling problem of (sub)-micrometric Pt-bearing nuggets during ablation by means

Table 2 Indexed SAED pattern obtained from Pt nanoparticles shown in Fig. 10

d-spacing (Å)	Pentlandite d-spacing (Å)	(<i>h k l</i>)	Platinum d-spacing (Å)	(<i>h k l</i>)
1.06	(0.05)	1.11	753	–
2.07	(0.02)	2.06	422	–
0.80	(0.11)	–	–	–
1.21	(0.01)	–	1.21	311
2.40	(0.09)	–	2.33	111
3.15	(0.05)	3.04	311	–
1.86	(0.06)	1.78	440	–
1.44	(0.11)	1.46	444	–

of LA–ICP–MS. The general interpretation is that Pt can be retained within the structure of MSS, but as the temperature is lower and the MSS re-equilibrates into pentlandite-pyrrhotite, the Pt will no longer can be accommodated and will form separate mineral aggregates (e.g., Makovicky et al. 1986; Fonseca et al. 2009; Wainwright et al. 2016). However, LA–ICP–MS analyses carried out here drilled the whole sulfide grain while analysing the Pt-rich nanoparticles (Fig. 5), leading us to conclude that the Pt-negative anomaly observed in our sulfide grains hosting Pt-rich nanoparticles is not analytically biased.

Detailed inspection of this type of pentlandite exhibiting Pt-negative anomaly by means of FIB/HRTEM indicates that Pt-rich nanoparticles hosted within it lack common orientation of the lattice fringes and the lack of gradational changes in the contents of Pt, Fe, and Cu with the crystalline pentlandite host (Figs. 6, 7, 8, 9, 10). This excludes the possibility that Pt-rich nanoalloys were exsolved from a solid BMS upon cooling. Rather, these Pt-rich alloy nanoparticles are polycrystalline, i.e., consists of aggregates formed by smaller crystals < 10 nm (Figs. 8a–c, 10), suggesting that these nanoparticles were formed by clustering of smaller Pt nanoparticles prior the crystallization of their hosting BMS. This suggests that in the absence of a semimetal partner (e.g., As, Sb or Bi) Pt may still self-organize itself or with Fe (and/or Cu) into physically separated phases within a sulfide melt, well before the concentration of this noble metal is high enough to form discrete minerals with other PGE. Nanoparticles involved in crystal seeding during nucleation could have been formed in either the sulfide melt itself (Wirth et al. 2013; Helmy et al. 2013; Junge et al. 2015) or in the silicate melt during crystallization/growth of the oxides as noted above. In these two scenarios, the already existing nanoparticles would be physically trapped by the droplets

of sulfide melt when the later were segregated as a result of local increases of fS_2 in the silicate melt. It is expected that partitioning of Pt-rich nanoparticles toward the sulfide liquid would be governed by surface properties and surface of the nano-associations, i.e., lower energy of the sulfide melt compared with the silicate melt. Taking into account that some experimental work indicates that at sulfide saturation the Pt alloys solubility is at the maximum at all fO_2 varying from IW to FMQ buffer (Fonseca et al. 2009; Mungall and Brenan 2014), one could expect that at any high temperature the alloy will readily dissolve upon contact with the sulfide matter. However, some of the particles analysed in this study do not show evidence of corrosion but perfectly well-developed faces and showing a good degree of crystallinity (Fig. 8a–c). This suggests that they remained as stable phases within the high-temperature melt consistent with phase relations in the Pt–Fe–Ni–S system predicting the formation of Pt and Pt–Fe alloys with Fe- and Ni-bearing sulfide melts in equilibrium at > 1100 – 1300 °C (e.g., Majzlan et al. 2002) and experiments reviewed by Pruseth and Palme (2004) where Pt and Pt–Fe nanoalloys also formed in Fe-rich sulfide melts at fO_2 defined by the FMQ buffer.

From the discussion above, an early partitioning of Pt as nanoparticles in both silicate and sulfide melts may explain Pt-depletion observed in some of the mantle-derived BMS analysed in this study and worldwide (Fig. 4). Moreover, if ascending magmas are subjected to changes in fO_2 and fS_2 , it is also expected that the segregating sulfide droplets and the matrix silicate melt should continuously re-equilibrate. Molten sulfide droplets entrained in the infiltrating alkali basaltic melt, eventually undergoing solidification, may have also been at some point subjected to decreasing fS_2 . This may have promoted their desulfurization and partial resorption, which also favored the saturation in Pt in some of the sulfide droplets as Pt-rich alloy nanoparticles (Peregoedova et al. 2004) as well as their transference towards the surrounding silicate melt. This is a complementary mechanism that may also explain the deficit of Pt relative to the other PGEs in many of the BMS containing Pt-rich nanoparticles (regardless if they are As-free or As-rich; Fig. 4) as well as the common occurrence of Pt-rich nanoalloys in the proximities of larger BMS in the interstitial silicate glass of the peridotite xenolith studied here.

The role of As in Pt-rich nanoparticles' crystallization process

Some of the BMS identified in the studied mantle xenoliths also contain inclusions of Pt–As (Fig. 3e–h; Appendix 1 in ESM). The observation that these Pt- and As-rich nanoparticles were only associated with BMS and not with silicate glass suggest a close link between As and the immiscible sulfide melts, consistent with the low capability of

the silicate melts to dissolve As (Hanley 2007). The fact that these BMS are devoid of Pt-rich alloy nanoparticles reflects: (1) destabilization of pre-existing Pt-rich alloy nanoparticles by reaction with small quantities of As present in some of the immiscible sulfide droplets, or alternatively (2) the preferential partitioning of Pt towards As eventually present in the droplets of sulfide melt rather than to Fe and Cu. In these cases, the fact that nanoscale partitioning of Pt in the sulfide melt is controlled by As instead of alloying confirms previous observations that Pt has stronger tendency towards As (i.e., chalcophile behavior) than for transition metals (Helmy and Bragagni 2017). Helmy et al. (2013) demonstrated that this mechanism may operate at nanoscale, as they were able to produce a series of non-crystalline $(Pt-As)_n$ polymolecular cluster, crystalline $PtAs_2$ nanoplatelets and immiscible Pt–As-rich melt nanoparticles in high-temperature (> 1000 °C) Ni–Fe sulfide melts. The uptake of Pt by nanoparticles that segregated earlier than formation of their host sulfide may also explain why BMS containing Pt–As nanoparticles also show strong negative anomalies of Pt relative to the other PGEs (Fig. 4). Our observation therefore confirms, at the nanoscale realm, previous empirical (Hanley 2007; Piña et al. 2015) and experimental observations (Helmy and Bragagni 2017; Bai et al. 2017) that Pt has stronger tendency towards As (i.e., chalcophile behavior) than for metal in Ni–Fe–Cu sulfide melts.

It is noteworthy that (sub)-micron-sized Pt-arsenides, including sperrylite ($PtAs_2$) have also been reported in other mantle BMS, including MSS, pentlandite, pyrrhotite, and chalcopyrite (e.g., Lorand et al. 2010; Alard et al. 2011). The interpretation given is that these Pt-arsenides were formed by the reaction between Pt-alloys or Pt-bismuthotellurides already existing in the BMS with As-bearing vapour phases, although once the BMS was solidified (e.g., Alard et al. 2011). Similarly these BMS hosting Pt–As phases also exhibit depletion in Pt relative to the other PGE (Fig. 4). Departing from our observations, there is no reason a priori to rule out the possibility that these Pt–As phases reported in other natural samples were also formed earlier than, or contemporaneously with, segregation of droplets of an immiscible sulphide melt instead than a post-solidus reaction of solid BMS with liquid or vapour phases. If so, Pt–As nano-association eventually present in the sulfide melt could coalesce acting as a seeds for the crystallization of larger micrometric Pt-arsenides (e.g., sperrylite) that are commonly found associated with many mantle BMS (Luguet and Reisberg 2016). Statistically, it is easier for a trace mineral to crystallize and grow if it can build on pre-existing nano-associations, than by assembling species randomly distributed in the melt (Helmy et al. 2013). If our interpretation is correct, it would confirm recent experimental works showing that sperrylite can crystallize from Ni–Fe–Cu sulfide melts

at > 900–1200 °C over the fO_2 of most terrestrial basalts (FMQ to FMQ -2; Canali et al. 2017; Bai et al. 2017).

Conclusions

1. Clusters of Pt nanoparticles could be physically fractionated as isolated refractory phases in high-temperature silicate and sulfide melts. Pt-rich alloy nanoparticles may form in both silicate and/or sulfide melts at high temperatures, whereas Pt–As nanocompounds preferentially form in sulfide melts. These observations suggest that many of the nanoparticles documented in other mantle sulfides, which were interpreted as due to exsolution upon cooling, may instead be magmatic in origin. Therefore, interpretation of the post-magmatic origin of Pt-rich (nano)-PGMs from many other geological suites may need to be reconsidered.
2. In the mantle, Pt-rich nanoparticles that segregated at very early magmatic stages could be attached to oxide–sulfide molten droplets/crystals dispersed in ascending silicate melts, imposing their Pt inventory to the extracted basaltic melt. Therefore, a significant control on Pt fractionation in mantle-derived magmas en route towards the overlying crust could be exerted by Pt-rich nanoparticles in their source, which may increase the availability of Pt, or have the opposite effect by reducing the budget of this metal in basaltic melts that could eventually undergo sulfide immiscibility. Good examples of this process are indeed provided by the presence of Pt-rich inclusions in Cr-spinel hosted in rapidly cooled picritic and ankaramitic lavas from Vanuatu and Urals (Kamenetsky et al. 2015). These magmas, originated from the upper mantle, reached the crust in S-undersaturated conditions and are considered to represent the parental melt of spatially and temporally associated platinumiferous peridotite bodies (Kamenetsky et al. 2015).
3. The confirmation that Pt-rich nanoparticles can form or be stable in high-temperature sulfide melts suggests that the association between Pt (and probably other PGE) and sulfide melts is related not only with chemical but also physical processes, given the tendency of nanoparticles of this metal to concentrate along with magmatic BMS. Interestingly, nano and micro-sized Pt-rich minerals have also been reported in sulfide globules (former droplets of sulfide melt) sealed in primitive olivine phenocrysts from island arc magma (high-Mg basalts produced by the 1941 eruption of Tolbachik volcano) (Zelensky et al. 2017). In the latter case the PGE minerals (particles) were crystallised directly from silicate melt serving as nucleation sites for sulfide droplets. These observations are relevant for our current understanding on the generation of magmatic PGE deposits

since that the accepted model for PGE concentration in these types of ores is based nearly exclusively on the sulfide/silicate partition coefficients, an assertion that must be reevaluated.

Acknowledgements The authors are grateful to D. Kamenetsky, Dave Holwell and an anonymous reviewer for their criticism that greatly improved our manuscript. We also acknowledge Associate Editor Chris Ballhaus for careful editorial handling. This research was supported by Spanish projects: RTI2018-099157-A-I00 and CGL2015-65824-P granted by the “Ministerio de Ciencia, Innovación y Universidades” and Ministerio de Economía y Competitividad” (MINECO), respectively. Additional funding for LA–ICP–MS analysis was provided by the Ramón y Cajal Fellowship RYC-2015-17596 to JMGJ. This study also contributes to the DID-UACH project #S-2015-52 to M. Schilling and the PhD project (S. Tassara) at University of Chile supported by the CONICYT Award scholarship #21170857. A. Jiménez is supported with a postdoctoral grant from the National Council on Science and Technology (CONACYT) of Mexico. Jesús Montes is acknowledged for preparation of thin sections. Trifon Trifonov (Polytechnic University of Catalonia), Rocío Márquez and María del Mar Abad (CIC of the University of Granada) and Malcolm P. Roberts (CMCA of the University of Western Australia) and Rosanna Murphy (GAU of Macquarie University) are acknowledged for their assistance with FIB, FESEM, HRTEM and EMPA, respectively.

References

- Alard O, Griffin WL, Lorand J-P, Jackson SE, O'Reilly SY (2000) Non-chondritic distribution of the highly siderophile elements in mantle sulphides. *Nature* 407:891–894
- Alard O, Griffin WL, Pearson NJ, O'Reilly SY (2002) New insights into the Re–Os systematics of sub-continental lithospheric mantle from in situ analysis of sulphides. *Earth Planet Sci Lett* 203:651–663
- Alard O, Lorand JP, Reisberg L, Bodinier JL, Dutria JM, O'Reilly SY (2011) Volatile-rich metasomatism in Monteferrier xenoliths (Southern France): consequence for chalcophile and highly siderophile element abundance in an orogenic-type subcontinental mantle segment. *J Pet* 5:6. <https://doi.org/10.1093/petrology/egr038>
- Amossé J, Allibert M, Fisher W, Piboule M (1990) Experimental study of the solubility of platinum and iridium in basic silicate melts—implications for the differentiation of platinum-group elements during magmatic processes. *Chem Geol* 81:45–53
- Amossé J, Dable P, Allibert M (2000) Thermochemical behavior of Pt, Ir, Rh and Ru vs. fO_2 and fS_2 in a basaltic melt. Implications for the differentiation and precipitation of these elements. *Miner Pet* 68:9–62
- Anenburg M, Mavrogenes JA (2016) Experimental observations on noble metal nanonuggets and Fe–Ti oxides, and the transport of platinum group elements in silicate melts. *Geochim Cosmochim Acta* 192:258–278
- Arguin J-P, Pagé P, Barnes S-J, Yu S-Y, Song X-Y (2016) The effect of chromite crystallization on the distribution of Osmium, Iridium, Ruthenium and Rhodium in Picritic Magmas: an example from the Emeishan large igneous province, Southwestern China. *J Pet* 57:1019–1048
- Armstrong JT (1988) Quantitative analysis of silicates and oxide minerals: comparison of Monte-Carlo, ZAF and Phi-Rho-Z procedures. In: Newbury DE (ed) *Microbeam analysis*. San Francisco Press, Inc., San Francisco, pp 239–246

- Aulbach S, Mungall JE, Pearson DG (2016) Distribution and processing of highly siderophile elements in cratonic mantle lithosphere. *Rev Miner Geochem* 81:239–304
- Bai L, Barnes S-J, Baker DR (2017) Sperrylite saturation in magmatic sulfide melts: implications for formation of PGE-bearing arsenides and sulfarsenides. *Am Miner* 102:966–974
- Ballhaus C, Sylvester P (2000) Noble metal enrichment processes in the Merensky Reef, Bushveld complex. *J Pet* 41:545–561
- Ballhaus C, Tredoux M, Späth A (2001) Phase relations in the Fe–Ni–Cu–PGE–S system at magmatic temperature and application to massive sulfide ores of the Sudbury igneous complex. *J Pet* 42:1911–1926
- Ballhaus C, Bockrath C, Wohlgemuth-Ueberwasser C, Laurenz V, Berndt J (2006) Fractionation of the noble metals by physical processes. *Contrib Miner Pet* 152:667–684
- Barnes S, Fisher AL, Godel B, Pearce M, Maier W, Paterson W, Howard D, Ryan C, Laird J (2016) Primary cumulus platinum minerals in the Monts de Cristal Complex, Gabon: magmatic micro-environments inferred from high-definition X-ray fluorescence microscopy. *Contrib Miner Pet* 171:23. <https://doi.org/10.1007/s00410-016-1232-1>
- Bennet NR, Brenan JM, Koga KT (2014) The solubility of platinum in silicate melt under reducing conditions: results from experiments without metal inclusions. *Geochim Cosmochim Acta* 133:422–442
- Borisov A, Palme H (1995) The solubility of iridium in silicate melts: new data from experiments with Ir10Pt90 alloys. *Geochim Cosmochim Acta* 59:481–485
- Borisov A, Palme H (1997) Experimental determination of the solubility of platinum in silicate melts. *Geochim Cosmochim Acta* 61:4349–4357
- Borisov A, Palme H (2000) Solubilities of noble metals in Fe containing melts as derived from experiments in Fe-free systems. *Am Miner* 85:1665–1673
- Brey GP, Köhler TP (1990) Geothermobarometry in four-phase lherzolites; II, new thermobarometers, and practical assessment of existing thermobarometers. *J Petrol* 31:1353–1378
- Canali AC, Brenan JM, Sullivan NA (2017) Solubility of platinum-arsenide melt and sperrylite in synthetic basalt at 0.1 MPa and 1200 °C with implications for arsenic speciation and platinum sequestration in mafic igneous systems. *Geochim Cosmochim Acta* 216:153–168
- Coltorti M, Beccaluva L, Bonadiman C, Salvini L, Siena F (2000) Glasses in mantle xenoliths as geochemical indicators of metasomatic agents. *Earth Planet Sci Lett* 183:303–320
- Cottrell E, Walker D (2006) Constraints on core formation from Pt partitioning in mafic silicate liquids at high temperatures. *Geochim Cosmochim Acta* 70:1565–1580
- Craig JR, Kullerud G (1969) Phase relations in the Cu–Fe–Ni–S system and their application to magmatic ore deposits. *Econ Geol Monogr* 4:344–358
- Ding K (1980) Further-studies of the minerals isoplatinocopper and hongshiite. *Sci Geol Sin* 2:167
- Donovan JJ, Snyder DA, Rivers ML (1993) An improved interference correction for trace element analysis. *Microbeam Anal* 2:23–28
- Donovan JJ, Singer JW, Armstrong JT (2016) A new EPMA method for fast trace element analysis in simple matrices. *Am Miner* 101:1839–1853
- Ertel W, Walter MJ, Drake MJ, Sylvester PJ (2006) Experimental study of platinum solubility in silicate melt to 14 GPa and 2273 K: implications for accretion and core formation in Earth. *Geochim Cosmochim Acta* 70:2591–2602
- Ertel W, Dingwell DB, Sylvester PJ (2008) Siderophile elements in silicate melts—a review of the mechanically assisted equilibration technique and the nanonugget issue. *Chem Geol* 248:119–139
- Féraud G, Alric V, Fornari M, Bertrand H, Haller M (1999) $^{40}\text{Ar}/^{39}\text{Ar}$ dating of the Jurassic volcanic province of Patagonia: migrating magmatism related to Gondwana break-up and subduction. *Earth Planet Sci Lett* 172:83–96
- Finnigan CS, Brenan JM, Mungall JE, McDonough WF (2008) Experiments and models bearing on the role of chromite as a collector of platinum group minerals by local reduction. *J Pet* 49:1647–1665
- Fleet ME, Pan Y (1994) Fractional crystallization of anhydrous sulfide liquid in the system Fe–Ni–Cu–S, with application to magmatic sulfide deposits. *Geochim Cosmochim Acta* 58:3369–3377
- Fonseca ROC, Campbell IH, O’Neill H, St C, Allen CM (2009) Solubility of Pt in sulphide mattes: implications for the genesis of PGE-rich horizons in layered intrusions. *Geochim Cosmochim Acta* 73:5764–5777
- Forsythe RD, Nelson EP, Carr MJ, Kaeding ME, Hervé M, Mpodozis C, Soffia JM, Harambour S (1986) Pliocene near-trench magmatism in southern Chile: a possible manifestation of ridge collision. *Geology* 14:23–27
- González-Jiménez JM, Reich M (2017) An overview of the platinum-group element nanoparticles in mantle-hosted chromite deposits. *Ore Geol Rev* 8:1236–1248
- González-Jiménez JM, Villaseca C, Griffin WL, O’Reilly SY, Belousova E, Ancochea E, Pearson NJ (2014) Significance of ancient sulphides PGE and Re–Os signatures in the mantle beneath Calatrava, Central Spain. *Contrib Miner Pet* 168:1047
- González-Jiménez JM, Deditius A, Gervilla F, Reich M, Suvorova A, Roberts MP, Roqué J, Proenza JA (2018) Nanoscale partitioning of Ru, Ir, and Pt in base-metal sulfides from the Caridad chromite deposit, Cuba. *Am Miner* 103:1208–1220
- Gorring ML, Kay SM (2000) Carbonatite metasomatized peridotite xenoliths from southern Patagonia: implications for lithospheric processes and Neogene plateau magmatism. *Contrib Miner Pet* 140:55–72
- Hanley J (2007) The role of Arsenic-rich melts and mineral phases in the development of high grade Pt–Pd mineralization within komatiite-associated magmatic Ni–Cu sulfide horizons at Dundonald Beach South, Abitibi Subprovince, Ontario, Canada. *Econ Geol* 102:305–317
- Helmy HM, Bragagni A (2017) Platinum-group elements fractionation by selective complexing, the Os, Ir, Ru, Rh-arsenide-sulfide systems above 1020 C. *Geochim Cosmochim Acta*. <https://doi.org/10.1016/j.gca.2017.01.040>
- Helmy HM, Ballhaus C, Fonseca ROC, Wirth R, Nagel T, Tredoux M (2013) Noble metal nanoclusters and nanoparticles precede mineral formation in magmatic sulphide melts. *Nat Commun*. <https://doi.org/10.1038/ncomms3405>
- Holwell DA, McDonald I (2010) A review of the behaviour of platinum group elements within natural magmatic sulfide ore systems. *Platin Metals Rev* 54:26–36
- Holwell DA, Keays RR, McDonald I, Williams MR (2015) Extreme enrichment of Se, Te, PGE and Au in Cu sulfide microdroplets: evidence from LA–ICP–MS analysis of sulphides in the Skaergaard Intrusion, east Greenland. *Contrib Mineral Petrol* 170:53
- Junge M, Wirth R, Oberthür T, Melcher F, Schreiber A (2015) Mineralogical sitting of platinum-group elements in pentlandite from the Bushveld Complex, South Africa. *Miner Depos* 50:41–54
- Kamenetsky VS, Park J-W, Mungall JE, Pushkarev EV, Ivanov AV, Kamenetsky MB, Yaxley GM (2015) Crystallization of platinum-group minerals from silicate melts: evidence from Cr-spinel-hosted inclusions in volcanic rocks. *Geology* 43:903–906
- Kitakaze A, Machida T, Komatsu R (2016) Phase relations in the Fe–Ni–S system from 875 to 650 & #xB0;C. *Can Miner* 54:1175–1186
- Köhler TP, Brey GP (1990) Calcium exchange between olivine and clinopyroxene calibrated as a geothermobarometer for natural

- peridotites from 2 to 60 kb with applications. *Geochim Cosmochim Acta* 54:2375–2388
- Kosyakov VI, Sinyakova F (2012) Physicochemical prerequisites for the formation of primary orebody zoning at copper-nickel sulfide deposits (by the example of the systems Fe–Ni–S and Cu–Fe–S). *Russ Geol Geophys* 53:861–882
- Kwitko R, Cabral AR, Lehmann B, Laflamme JHG, Cabri LJ, Criddle AJ, Galbiatti HF (2002) Hongshiite, PtCu, from itabirite-hosted Au–Pd–Pt mineralization (Jacutinga), Itabira district, Minas Gerais, Brazil. *Can Mineral* 40:711–723
- Laurora A, Mazzucchelli M, Rivalenti G, Vannucci R, Zanetti A, Barbieri MA, Cingolani C (2001) Metasomatism and melting in carbonated peridotite xenoliths from the mantle wedge: the Gobernador Gregores case (Southern Patagonia). *J Pet* 42:69–87
- Li C, Barnes S-J, Makovicky E, Rose-Hansen J, Makovicky M (1996) Partitioning of nickel, copper, iridium, rhodium, platinum and palladium between monosulphide solid solution and sulphide liquid: effects of composition and temperature. *Geochim Cosmochim Acta* 60:1231–1238
- Liu Y, Brenan J (2015) Partitioning of platinum-group elements (PGE) and chalcogens (Se, Te, As, Sb, Bi) between monosulfide-solid solution (MSS), intermediate solid solution (ISS) and sulfide liquid at controlled fO_2 – fS_2 conditions. *Geochim Cosmochim Acta* 159:139–161
- Lorand JP, Alard O, Lugué A (2010) Platinum-group element micronuggets and refertilization process in Lherz orogenic peridotite (northeastern Pyrenees, France). *Earth Planet Sci Lett* 289:298–310
- Lorand J-P, Lugué A, Alard O (2013) Platinum-group element systematics and petrogenetic processing of the continental upper mantle: a review. *Lithos* 164–167:2–21
- Lugué A, Reisberg L (2016) Highly siderophile element and 187Os signatures in non-cratonic basalt-hosted peridotite xenoliths: unravelling the origin and evolution of the post-archean lithospheric mantle. *Rev Miner Geochem* 81:305–367
- Majzlan J, Makovicky M, Makovicky E, Rose-Hansen J (2002) The system Fe–Pt–S at 1100 °C. *Can Miner* 40:509–517
- Makovicky M, Makovicky E, Rose-Hansen J (1986) Experimental studies on the solubility and distribution of platinum group elements in base metal sulphides in platinum deposits. In: Neary CR, Priedhard HM, Gallagher MJ, Ixer RA (eds) *Metallurgy of basic and ultrabasic rocks*. The Institution of Mining and Metallurgy, London, pp 415–425
- Mansur ET, Barnes S-J, Duran C (2019) Textural and compositional evidence for the formation of pentlandite via peritectic reaction: implications for the distribution of highly siderophile elements. *Geology*. <https://doi.org/10.1130/G45779.1>
- Médard E, Schmidt MW, Wälle M, Keller NS, Günther D (2015) Platinum partitioning between metal and silicate melts: core formation, late veneer and the nanonuggets issue. *Geochim Cosmochim Acta* 162:183–201
- Mungall JE, Brenan JM (2014) Partitioning of platinum-group elements and Au between sulfide liquid and basalt and the origins of mantle-crust fractionation of the chalcophile elements. *Geochim Cosmochim Acta* 125:265–289
- Pankhurst RJ, Riley TR, Fanning CM, Kelley SP (2000) Episodic silicic volcanism in Patagonia and the Antarctic Peninsula: chronology of magmatism associated with the break-up of Gondwana. *J Pet* 41:605–625
- Peregoedova A, Barnes SJ, Baker DR (2004) The formation of Pt–Ir alloys and Cu–Pd-rich sulfide melts by partial desulfurization of Fe–Ni–Cu sulfides: results of experiments and implications for natural systems. *Chem Geol* 208:247–264
- Piña R, Gervilla F, Barnes S-J, Ortega L, Lunar R (2015) Liquid immiscibility between arsenide and sulfide melts: evidence from a LA–ICP–MS study in magmatic deposits at Serranía de Ronda (Spain). *Miner Depos* 50:265–279
- Pruseth KL, Palme H (2004) The solubility of Pt in liquid Fe-sulfides. *Chem Geol* 208:233–245
- Riley TR, Leat PT, Pankhurst RJ, Harris C (2001) Origin of large volume rhyolitic volcanism in the Antarctic Peninsula and Patagonia by crustal melting. *J Pet* 42:1043–1065
- Roeder PL, Jamieson HE (1992) Composition of chromite and co-existing Pt–Fe alloy at magmatic temperatures. *Aust J Earth Sci* 39:419–426
- Saunders JE, Pearson NJ, O'Reilly SY, Griffin WL (2015) Sulphide metasomatism and the mobility of gold in the lithospheric mantle. *Chem Geol* 410:149–161
- Saunders JE, Pearson NJ, O'Reilly SY, Griffin WL (2016) Gold in the mantle: the role of pyroxenites. *Lithos* 244:205–217
- Scamberulli M, Vannucci R, De Stefano A, Preite-Martinez M, Rivalenti G (2009) CO₂ fluid and silicate glass as monitors of alkali basalt/peridotite interaction in the mantle wedge beneath Gobernador Gregores, Southern Patagonia. *Lithos* 107:121–133
- Schilling M, Conceição RV, Mallmann G, Koester E, Kawashita K, Hervé F, Morata D, Motoki A (2005) Spinel-facies mantle xenoliths from Cerro Redondo, Argentine Patagonia: petrographic, geochemical, and isotopic evidence of interaction between xenoliths and host basalt. *Lithos* 82:485–502
- Schilling ME, Carlson RW, Conceição RV, Dantas C, Bertotto GW, Koester E (2008) Re–Os isotope constraints on subcontinental lithospheric mantle evolution of southern South America. *Earth Planet Sci Lett* 268:89–101
- Schilling ME, Carlson RW, Tassara A, Conceição RV, Bertotto GW, Vásquez M, Muñoz D, Jalowitzki T, Gervasoni F, Morata D (2017) The origin of Patagonia revealed by Re–Os systematics of mantle xenoliths. *Precambrian Res* 294:15–32
- Stern CR, Frey FA, Futa K, Zartman RE, Peng Z, Kyser TK (1990) Trace-element and Sr, Nd, Pb, and O isotopic composition of Pliocene and Quaternary alkali basalts of the Patagonia Plateau lavas of southernmost South America. *Contrib Miner Petrol* 104:294–308
- Sugaki A, Kitakaze A (1998) High form of pentlandite and its thermal stability. *Am Miner* 83:133–140
- Tassara S, González-Jiménez JM, Reich M, Schilling ME, Morata D, Begg G, Saunders E, Griffin WL, O'Reilly SY, Grégoire M, Barra F, Corgne A (2017) Plume-subduction interaction forms large auriferous provinces. *Nat Commun* 8:843
- Tassara S, González-Jiménez JM, Reich M, Saunders E, Lugué A, Morata D, Grégoire M, van Acken D, Schilling ME, Barra F, Nowell G, Corgne A (2018) Highly siderophile elements mobility in the subcontinental lithospheric mantle beneath southern Patagonia. *Lithos* 314–315:579–596
- Taylor W (1998) An experimental test of some geothermometer and geobarometer formulations for upper mantle peridotites with application to the thermobarometry of fertile Iherzolite. *Neues Jahrbuch für Miner Abhandlungen* 172(2/3):381–408
- Tredoux M, Lindsay NM, Davies G, McDonald L (1995) The fractionation of platinum-group elements in magmatic systems, with the suggestion of a novel causal mechanism. *S Afr J Geol* 98:157–167
- Wainwright AN, Lugué A, Schreiber A, Fonseca ROC, Nowell GM, Lorand J-P, Wirth R, Janney PE (2016) Nanoscale variations in ¹⁸⁷Os isotopic composition and HSE systematics in a Bultfontein peridotite. *Earth Planet Sci Lett* 447:60–71
- Waldner P, Pelton AD (2004) Critical thermo-dynamic assessment and modeling of the Fe–Ni–S system. *Metall Mater Trans B* 35:897–907
- Wang KL, O'Reilly SY, Griffin WL, Pearson NJ, Zhang M (2009) Sulfides in mantle peridotites from Penghu Island, Taiwan: melt percolation, PGE fractionation, and the lithospheric evolution of the South China block. *Geochim Cosmochim Acta* 73:4531–4557

Wilson AH, Tredoux M (1990) Lateral and vertical distribution of the platinum-group elements, and petrogenetic controls on the sulphide mineralisation in the P1 Pyroxenite Layer of the Darwendale Subchamber of the Great Dyke, Zimbabwe. *Econ Geol* 85:556–584


Wirth R, Reid D, Schreiber A (2013) Nanometer-sized platinum-group minerals (PGM) in base metal sulfides: new evidence for an orthomagmatic origin of the Merensky Reef PGE ore deposit, Bushveld Complex, South Africa. *Can Miner* 51:143–155

Zelensky M, Kamenetsky VS, Navrogenes JA, Danyushevsky LV, Matveev D, Gurenko AA (2017) Platinum-group elements and

gold in sulfide melts from modern arc basalt (Tolbachik volcano, Kamchatka). *Lithos* 290–291:172–188

Publisher's Note Springer Nature remains neutral with regard to jurisdictional claims in published maps and institutional affiliations.

Affiliations

José María González-Jiménez¹  · Josep Roqué-Rosell^{2,3} · Abigail Jiménez-Franco^{2,3,4} · Santiago Tassara⁵ · Fernando Nieto^{1,6} · Fernando Gervilla^{1,6} · Sandra Baurier^{2,3} · Joaquín A. Proenza^{2,3} · Edward Saunders⁷ · Artur P. Deditius⁸ · Manuel Schilling⁹ · Alexandre Corgne⁹

¹ Departamento de Mineralogía y Petrología, Facultad de Ciencias, Universidad de Granada, Avda. Fuentenueva s/n, 18002 Granada, Spain

² Departament de Mineralogia, Petrologia i Geologia Aplicada, Facultat de Ciències de la Terra, Universitat de Barcelona, 08028 Barcelona, Spain

³ Institut de Nanociència i Nanotecnologia, IN2UB Facultat de Química, Universitat de Barcelona, Av. Diagonal 645, 08028 Barcelona, Spain

⁴ Posgrado en Ciencias de la Tierra, Universidad Nacional Autónoma de México, Ciudad Universitaria, Delegación Coyoacán, 04510 Mexico City, Mexico

⁵ Department of Geology and Andean Geothermal Center of Excellence (CEGA), Universidad de Chile, 8370450 Santiago, Chile

⁶ Instituto Andaluz de Ciencias de la Tierra (IACT), Universidad de Granada-CSIC, 18100 Granada, Spain

⁷ Division of Earth Sciences, School of Environmental and Rural Science, University of New England, Armidale, NSW 2351, Australia

⁸ School of Engineering and Information Technology, Murdoch University, Murdoch, WA 6150, Australia

⁹ Instituto de Ciencias de la Tierra, Universidad Austral de Chile, 5090000 Valdivia, Chile